



Investigation on the effect of the gas-to-metal ratio on powder properties and PBF-LB/M processability

S. Cacace¹ · M. Boccadoro² · Q. Semeraro¹

Received: 6 February 2023 / Accepted: 15 July 2023
© The Author(s) 2023

Abstract

Metal powders for the laser powder bed fusion process are usually produced via gas atomization. However, due to the tight particle size distribution required for this application, the yield of the atomization process is low, resulting in a high-powder cost. In this work, atomization process parameters were varied to increase the gas-to-metal ratio to reduce the particle size distribution produced, and therefore increase the yield of the process. As a result, eight powders were produced starting from scrap AISI 136L material at different gas-to-metal ratio values, and the atomization process yield was successfully increased by 50%. First, the eight powders were characterized in terms of powder size, shape distributions, and flowability. Later, all powders were used to produce tensile specimens. The powders produced at higher yield exhibited a larger number of fine particles but slightly lower circularity, particularly in the coarse fraction. Furthermore, powders produced at a high gas-to-metal ratio demonstrated enhanced flowing properties and higher packing density. Consequently, these powders exhibited superior tensile performance, with ultimate tensile strength (UTS) ranging from 651 to 673 MPa and elongation values between 63 and 66%.

Keywords Vacuum-induced gas atomization · Flowability · Scrap material · Laser powder bed fusion

Abbreviations

CED	Circular equivalent diameter (μm)
CBD	Conditioned bulk density (g/mL)
D_{eq}	Equivalent spherical diameter (μm)
GMR	Gas-to-metal ratio
PBF-LB/M	Laser powder bed fusion of metals
SE	Specific energy (MJ/g)

1 Introduction

Laser powder bed fusion of metals (PBF-LB/M) is one of the most widespread additive manufacturing (AM) techniques in industrial production. PBF-LB/M technology consists of a laser beam that selectively melts powder fed layer by layer in a sealed chamber filled with inert gas. To achieve a broader industrial adoption, the PBF-LB/M process must

be competitive with conventional manufacturing in terms of costs, productivity, and material availability [1]. However, there exist significant challenges to overcome, particularly in reducing costs and production time associated with this technology. PBF-LB/M has high capital and operative expenses generated by machine purchase, inert gas consumption, and risk of build failure due to process instability, post-processing, and powder procurement [2]. Powder price is a non-negligible cost driver for additive manufacturing users, accounting for ~10% of the total production expense [3, 4].

From the perspective of powder suppliers, significant effort is dedicated to the atomization process. However, after sieving, only a small portion of the powder (less than 50%, [5]) meets the size requirements for sale in the PBF-LB/M market. This limitation arises because the atomization process inherently produces powder particles within the 0–500 μm range, while PBF-LB/M necessitates a narrow particle size distribution (PSD) ranging from 10 to 60 μm . As a result, the low yield and reduced energy efficiency of the atomization process contribute to inflated powder prices. Moreover, careful atomization can yield powders with tailored particle shapes and sizes, which positively influence powder flow behavior. This, in turn, enables faster printing speeds and reduces overall process time and costs [6, 7].

✉ S. Cacace
stefania.cacace@polimi.it

¹ Dipartimento di Meccanica, Politecnico di Milano, Via La Masa 1, 20156 Milano, Italy

² Tenova S.p.A., Via Gerenzano 58, 21053 Castellanza, Italy

Therefore, further research is necessary to encourage industrial applications by reducing costs and meeting higher sustainability goals in the additive manufacturing (AM) supply chain [8]. Achieving the right combination of atomization parameters can effectively reduce the particle size range produced during atomization, leading to an increased process yield for PBF-LB/M applications. Studies focusing on the gas atomization process highlight the gas-to-metal ratio (GMR) as a key parameter directly influencing the particle size range. The GMR describes the energy input from the gas during atomization. Increasing the GMR results in greater interaction between the gas jet energy and the molten stream, leading to a decreased median particle size and a narrower distribution [9–11].

Generally, a higher gas-to-metal ratio (GMR) leads to an increased number of fine particles, which enhances the productivity of the atomization process for the desired powder range in PBF-LB/M processes. However, research on increasing the atomization yield specifically for PBF-LB/M applications is relatively new, and only a limited number of studies are available. Furthermore, most of the literature work focuses on general applications [12, 13] without considering the specific requirements of PBF-LB/M.

This study aims to investigate the impact of GMR on the powder quality produced for the PBF-LB/M process, as well as the resulting tensile properties of the printed specimens. The material chosen for atomization is AISI 316L metal scrap, which has been optimized in a previous work by the authors [14]. The objective is to assess whether improved atomization efficiency comes at the cost of decreased quality in the printed parts.

To achieve this, the nozzle ring of the atomizer was modified to enable an average increase in GMR of approximately

50%. Four powders were produced from the scrap AISI 316L material for each nozzle configuration (standard and enhanced).

The workflow of the work is presented in Fig. 1, and the paper is organized as follows: Sect. 2 discusses powder production and the powder and specimens characterization techniques. In Sect. 3, the powder analysis and tensile properties are reported and discussed.

2 Materials and methods

2.1 Atomization process

Industrial AISI 316L steel scrap with low contamination and oxidation was selected to produce powders for PBF-LB/M. A batch of AISI 316L scrap was melted by vacuum induction melting and atomized by vacuum inert gas atomization.

While attaining complete control over the particle size of gas-atomized powder is not feasible, it is possible to influence the particle size distribution by adjusting the atomization pressure, which directly affects the gas-to-metal ratio [15]. GMR is defined as:

$$\text{GMR} = \frac{\text{Gas flow rate}}{\text{Metal flow rate}} \quad (1)$$

The nozzle was modified to increase the gas flow rate, and therefore increase the GMR. The details of the specific nozzle modification cannot be disclosed due to a pending patent.

Some atomization parameters were fixed: argon (Ar) as inert atomization gas, overheating temperature of 180 °C, and nozzle diameter of 2 mm. The varied parameters are

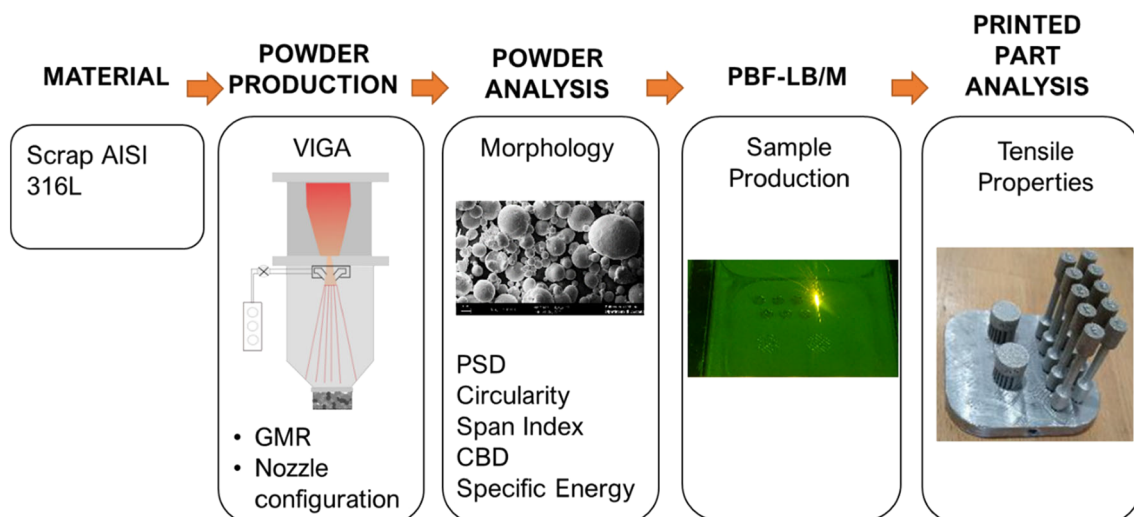


Fig. 1 Workflow of the experimentation

reported in Table 1. Batch 1 refers to the standard nozzle configuration, while batch 2 refers to the enhanced nozzle configuration.

The GMR is an efficiency index of gas consumption vs. the metal flow rate. Still, it does not consider how much of the produced powder is compliant with a specific range. The supplier considered the particle size range of 10–60 μm [16] compliant with PBF-LB/M. The atomization yield was defined as:

$$\text{yield} = \frac{\text{Initial metal charge}}{\text{LPBF compliant powder weight}} \quad (2)$$

PBF-LB/M compliant powder weight was obtained after proper sieving on the VIGA output. Atomization parameters corresponding to powder 2 in batch 1 (GMR equal to 1.3) are the standard ones to produce AISI 316L powders.

2.2 Laser powder bed fusion process

Powders were tested on an industrial PBF-LB/M system, Renishaw AM250. The machine is equipped with a 200 W fiber laser working in pulsed mode. The laser spot is approximately 70 μm at the focal position. The process parameters were optimized in previous work [14] which used the same input material for producing scrap AISI 316L for metal-AM technologies (Table 2).

Five tensile specimens for each powder and two cylindrical specimens (height 7 mm, diameter 15 mm) were printed. Tensile specimens were printed according to ASTM E8-16 standard (see Table 3 for the details). The cylindrical specimens were grinded on one side for chemical analysis. The other side was polished and etched for microstructural analysis. The tensile specimens were printed perpendicular to the building plate, this choice was made to study the worst case scenario in terms of mechanical properties [17].

Table 1 Variation of process parameters for the atomization experimental campaign

Batch	Powder	Atomization pressure [bar]	Gas flow rate [kg/s]	Metal flow rate [kg/s]	GMR [–]
1	1	53	0.1	0.06	1.7
	2	45	0.08	0.06	1.3
	3	53	0.1	0.05	2.2
	4	45	0.08	0.05	1.5
2	5	45	0.13	0.06	2.2
	6	53	0.16	0.05	3.1
	7	45	0.13	0.05	2.7
	8	53	0.16	0.04	3.9

2.3 Powder characterization

Particle morphology was qualitatively and quantitatively evaluated. SEM images were used to identify any significant defects resulting from the atomization process to quantitatively analyze the powders, the Malvern Morphologi 4 system was employed. This system captures images of individual powder particles dispersed on glass and generates size and shape distributions. Two repetitions were conducted for each powder. The images obtained using Morphologi 4 were analyzed using the proprietary software integrated with the microscope.

The analysis focused on specific morphological indexes derived from the particle area and perimeter. These indexes provided valuable information related to particle size, such as circular equivalent diameter (CED), as well as shape, such as circularity. The CED is evaluated as:

$$\text{CED} = 2\sqrt{\frac{\text{Area}}{\pi}} \quad (3)$$

The CED represents the diameter of a circle with the same areas as the 2D image of the particles. Circularity is evaluated as

$$\text{Circularity} = \frac{\text{Perimeter}}{\pi \times \text{CED}} \quad (4)$$

Circularity quantifies how close a shape is to a perfect circle. A circularity close to 0 indicates a highly elongated particle, while a perfect circle has a circularity equal to 1.0.

The span index was used to summarize the PSD results for each powder [18]; this index was evaluated as follows:

Table 2 Process parameters used for tensile specimens production

Process parameters	Unit	Value
Peak power	W	200
Exposure time	μs	80
Point distance	μm	60
Hatch distance	μm	100
Layer thickness	μm	50
Energy density	J/mm ³	53

Table 3 Tensile specimens geometry based on ASTM E8-16

Dimension	[mm]
G—Gauge length	16 ± 0.1
D—Diameter	4 ± 0.1
R—radius fillet, min	4
A—length of reduced section, min	20

$$\text{Span index} = \frac{D_{90} - D_{10}}{D_{50}} \quad (5)$$

where D_x represents the x^{th} -quantile of the particle size distribution. The larger the span index, the wider the PSD.

The result of the PSD measurement can be described in two ways: number-based distribution and volume-based distribution. The number-based distribution is the most straightforward: each particle accounts for its size (i.e., CED). In contrast, for the volume-based distribution, each particle accounts for its volume, meaning that larger particles weigh more than smaller ones. Morphologi software converts the number-based distribution into volume-based results based on the equivalent spherical volume of each particle (D_{eq}) [μm^3]. D_{eq} represents the volume of a sphere with a diameter equal to the CED of each particle. The spherical equivalent volume is calculated as follows:

$$D_{\text{eq}} = \frac{4}{3}\pi \sqrt[3]{\left(\frac{\text{Area}}{\pi}\right)^3} \quad (6)$$

Consequently, there can be discrepancies between the number-based and volume-based distributions. Usually, the laser diffraction method is employed to measure the PSD [19, 20]. Laser diffraction (LD) involves using a laser to irradiate the particles, which results in scattering in various directions. By analyzing the scattering pattern, information about the particle volume and equivalent diameter can be derived. The diameter of the particles measured using LD is derived from a volume value assuming a spherical shape for the particles. In this study, the volume-based distribution is used to compare the PSD microscopy results of this work with the commonly presented distributions in the PBF-LB/M literature. The number-based distribution is used to detect differences in the distribution of the actual size of the particles generated during the atomization process.

Rheology includes the static and dynamic behavior of the powder and its interaction with air [21]. The ability of the powder to flow and its packing properties are of interest for PBF-LB/M application. These characteristics were studied using Freeman Technology FT4, a universal powder flow tester. The dynamic flow characterization test was selected to describe the behavior of the produced powders using the 25 mm \times 25 mm vessel assembly. In detail, specific energy SE (mJ/g) and conditioned bulk density CBD (g/mL) were analyzed. SE measures how powder flows in an unconfined low-stress environment [22]. According to Fereiduni et al. [23] and Balbaa et al. [24], SE represents the powder flowability since the powder/blade interaction during the upward motion of the blade is closer to the powder/recoater interaction during the powder spreading stage in the PBF-LB/M process. CBD represents the packing density of the loose powder [23], and it represents an approximation

of the packing properties of the powder when spread. The dynamic flow characterization test was replicated three times for each powder following a random order.

2.4 Sample characterization

The specimen mechanical performance and microstructure were analyzed. For each powder, five samples were subjected to tensile tests. The measured properties were ultimate tensile strength (UTS, [MPa]), percentage elongation after fracture (e, [%]), Young modulus (E, [MPa]), and yield stress (YS, [MPa]). Fracture surfaces were observed with an SEM microscope. The two small cylindrical specimens for each powder were used to analyze the printed parts microstructure. The microstructure was observed using SEM EVO-50 (Carl-Zeiss) and an optical microscope. The specimens were grinded and etched (a mixture of water, hydrochloric acid, and nitric acid in equal parts).

3 Results and discussion

3.1 Powder properties

The atomization yield, as measured by Eq. 2, showed an increase from $\sim 38\%$ (which corresponds to the standard operating parameters for AISI 316L atomization) to $\sim 57\%$ (Table 4). It should be noted that each of the eight powders listed in Table 4 is the result of one atomization run, indicating the absence of replications for each combination of nozzle configuration and GMR.

In Fig. 2, a linear regression model is fit to the data to estimate the increase in yield as function of the GMR; the estimated equation is $\text{yield} = 34.15 + 5.90 \text{ GMR}$ with an $\text{adj-}R^2 = 87.96\%$. A unit increase in GMR produces a 5.9% increase in the yield of the atomization process. A 95% prediction interval was also calculated to show the robustness of the model. For a GMR equal to 2.2, two

Table 4 The yield of the atomization process as function of the GMR

Batch	Powder	GMR	Atomization yield [%]
1	1	1.7	46
	2	1.3	38
	3	2.2	47
	4	1.5	45
2	5	2.2	48
	6	3.1	51
	7	2.7	51
	8	3.9	57

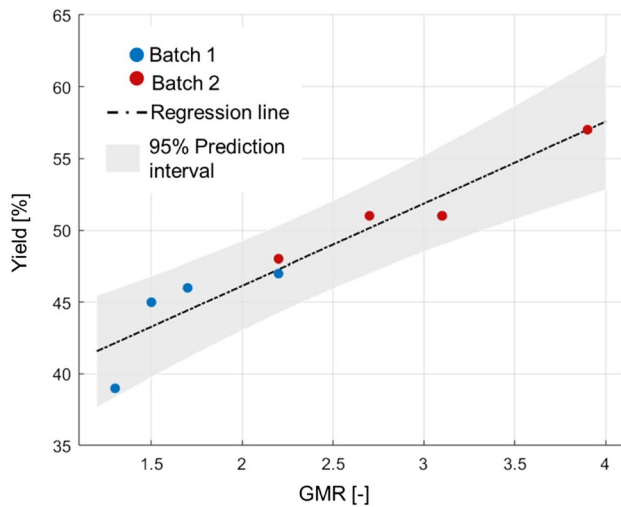


Fig. 2 Relationship between GMR and the atomization yield for the eight powders investigated in this study. The estimated equation is $\text{yield} = 34.15 + 5.90 \text{ GMR}$

atomization runs are available, one with the standard nozzle (batch 1) and another with the enhanced nozzle (batch 2). The resulting yields are 47% and 48%, respectively, indicating that the nozzle modification did not influence the relationship between the GMR and the expected yield [12].

The powder morphology was examined qualitatively using SEM, and quantitative analysis was conducted using the Malvern Morphologi 4 microscope. Powders in Fig. 3 exhibit a quasi-spherical shape, along with the presence of satellites, splat caps [25], and surface irregularities. These defects are commonly observed in powders produced through gas atomization [26]. The SEM images show a larger number of fine particles for powders atomized with the enhanced nozzle, while the standard configuration produces particles with greater circularity.

Particle size and circularity distributions are illustrated in Figs. 4 and 5, respectively. To ensure clarity, only one of the two replicated measurements is shown in both figures.

In Fig. 4a, the number-based CED distribution is displayed, which is not commonly found in the literature. This representation emphasizes the differences between the powders from batch 1 and batch 2 more than the volume-based CED distribution in Fig. 4b.

The powder produced in standard conditions (batch 1) shows a bi-modal number-based distribution (Fig. 4a). However, the corresponding volume-based distribution follows the typical log-normal shape. Based on the literature data on number-based distribution for PBF-LB/M processes, a peak of fine particles is expected [27, 28]. This result confirms that volume-based distributions can be misleading when fine particles are of interest, as suggested by Sutton et al. [19].

Powders produced with the enhanced nozzle (batch 2) show a high quantity of small quasi-spherical particles, aligning with the expected outcome of a higher gas-to-metal ratio [9, 29]. Additionally, batch 2 powders display a distinct peak of fine particles at around 5 μm and narrower size distribution. Summarized statistics of the particle size and circularity distributions are reported in Table 9 in the Appendix.

The circularity distributions presented in Fig. 5 also confirm the observations made through SEM analysis. Powders produced with the enhanced nozzle (powders 5 to 8) tend to exhibit less spherical particles, as indicated by lower circularity values. The increased gas pressure applied during the production of batch 2 powders results in a higher probability of collision between solidified smaller particles and nearly solidified larger droplets within the atomization chamber, resulting in the formation of satellites [30, 31]. This phenomenon explains why powder 3 from batch 1 and powder 5 from batch 2 show different number-based particle size distributions, despite sharing the same GMR value of 2.2. Powder 5 was produced with a higher gas flow rate, leading

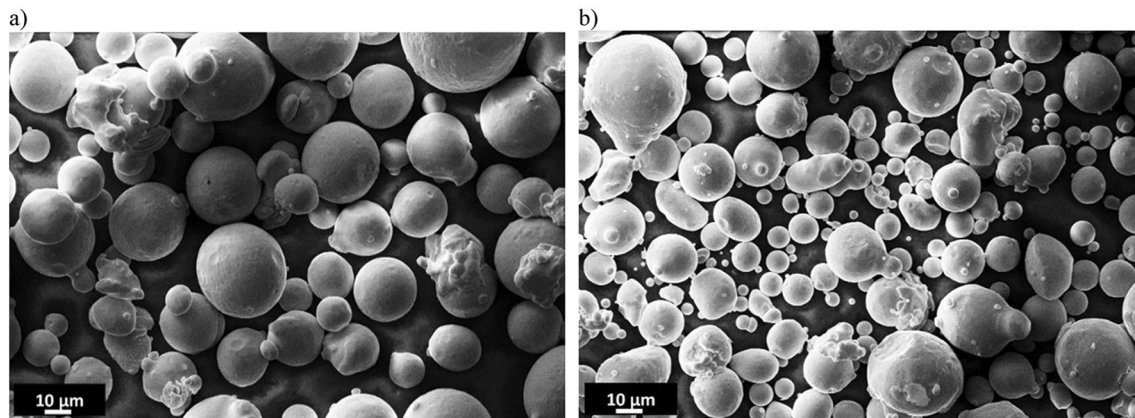


Fig. 3 SEM images of two reference powders from batch 1 (a) and batch 2 (b)

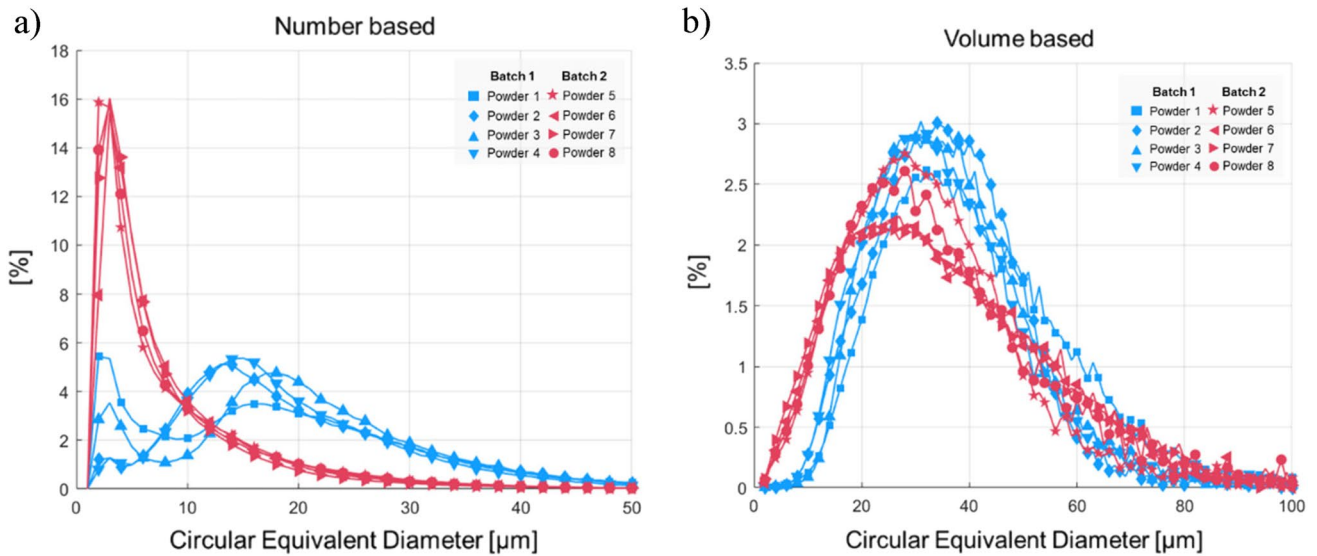


Fig. 4 Circular equivalent diameter (CED) for the eight powders **a** number-based, **b** volume-based. One of the two replicated measurements is shown

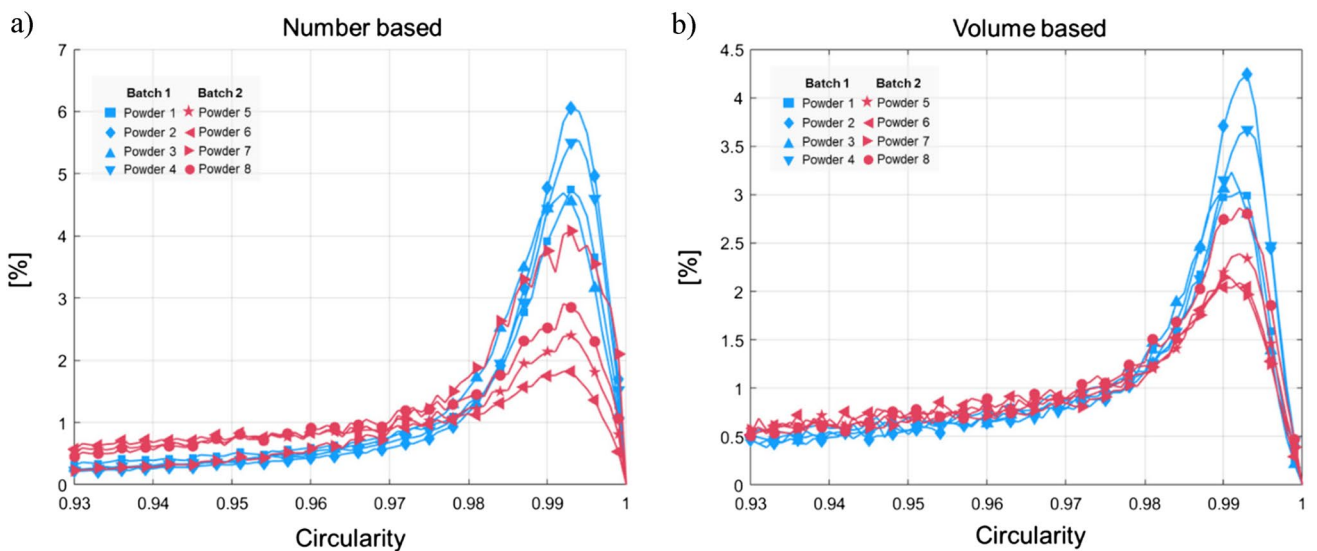


Fig. 5 Circularity for the eight powders **a** number-based and **b** volume-based distributions. One of the two replicated measurement is shown

to a more pronounced formation of fine powders compared to powder 3.

The histogram in Fig. 6 illustrates the circularity values of the larger fraction (CED-number larger than 50 μm) for powder 1 from batch 1 and powder 8 from batch 2. As visible, large particles produced with lower GMR show higher circularity, while for the same CED range, a higher GMR reduces the shape quality.

Table 5 presents the mean span index for both volume-based and number-based distributions. The span index serves as an indicator of the width of the particle size distribution. The span index values for powders from batch 2 are larger

than the ones for batch 1, which contradicts the previously mentioned relationship between GMR and PSD: larger GMR results in higher yield because of narrower PSD. The relationship is valid for the entire amount of powder produced from the atomization, while the values in Table 5 refer to the sieved fraction intended for PBF-LB/M application. The span index is also considered a good approximation of the powder flowability [18, 32], with values of span index > 1.5 resulting in lower flowing properties.

In Table 5, significant differences between the number-based and volume-based span index can be observed due to the distinct distributions depicted in Fig. 4a. The limit value

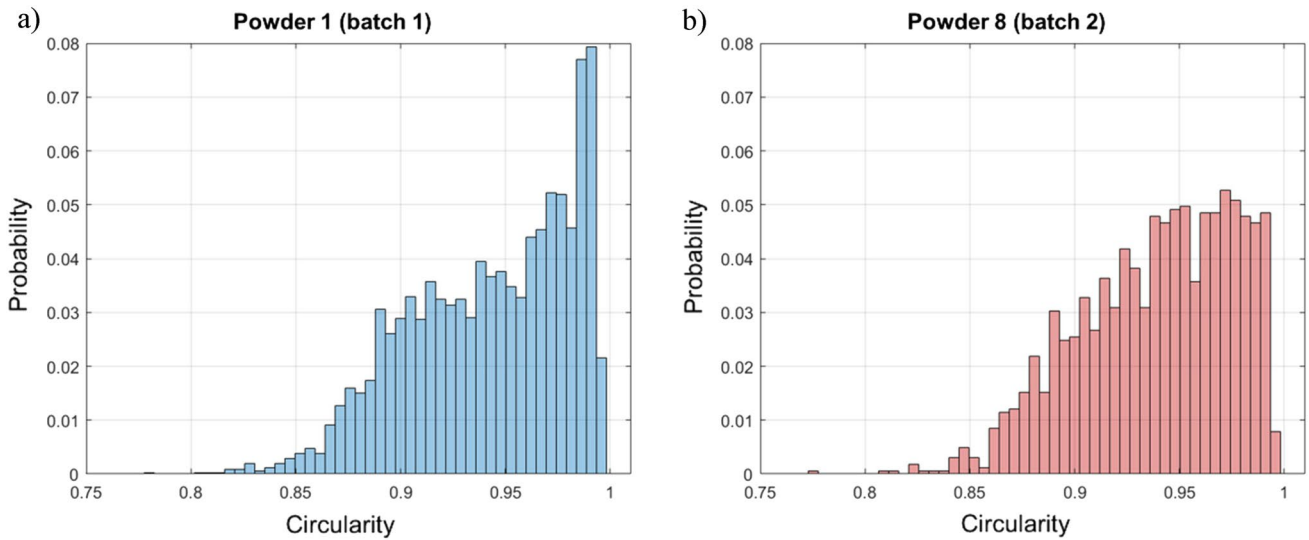


Fig. 6 Circularity values for particles with CED larger than 50 μm for a representative powder from batch 1 (a) and batch 2 (b). Only one powder for each batch was analyzed for practical purposes

Table 5 Volume-based and number-based span index values. For each powder, the mean value of the span index was reported based on two replicated measurements

Batch	Powder	Span index (volume based)	Span index (number-based)
1	1	1.11	1.87
	2	0.98	1.56
	3	1.04	1.40
	4	1.09	1.38
2	5	1.34	3.23
	6	1.48	2.87
	7	1.51	2.87
	8	1.44	3.13

of 1.5 in the span index is based on studies that measured the PSD with laser diffraction methods, so we should expect good flowing properties from all the powders because the volume-based span index range is [0.98;1.51].

The flowability characterization results are presented in Fig. 7, where each bar represents the mean of three measurements, and the error bars indicate the standard error. Powders produced with a higher GMR are characterized by higher packing density (high CBD) and improved flowability (low SE). CBD refers to the arrangement of particles within a given volume. A higher CBD value suggests better particle packing, implying a more uniform powder bed and lower presence of voids in the layer [33]. The difference between the two batches is more evident when examining

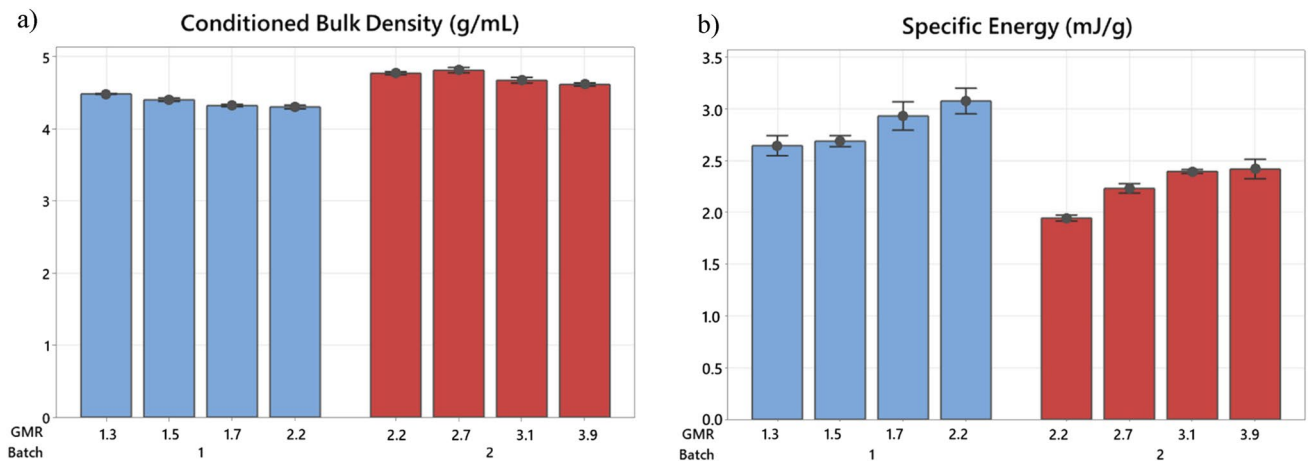


Fig. 7 Results of the flowability characterization, **a** conditioned bulk density CBD, **b** specific Energy SE

the SE values compared to CBD. A low SE indicates that less energy is required to induce a defined flowing pattern in the powder, thus corresponding to a higher flowability. As indicated by [34], a lower SE implies a better powder bed uniformity.

3.1.1 Discussion on powder characterization

In the literature, a widespread agreement cannot be found about the relationship between PSD, shape, and flowability. Some references [35, 36] claim that non-spherical particles may exhibit favorable flow behavior, especially for fine powders where adhesive forces are significant. Conversely, other authors [19] suggest that high sphericity promotes good flowability. Based on the results of this study, the presence of fine particles does not necessarily imply a lower flowability. Highly irregular water atomized steels were successfully processed via PBF-LB/M [37, 38], indicating a low particle shape influence on the processability of these materials. A larger CBD suggests a higher powder packing density, as the high number of fine particles fills the void between the larger ones, reducing the gaps within the powder bed. Powder packing density can be evaluated by comparing CBD to the density of the bulk material (7.98 g/L). Among the powder tested, powder 4 exhibits the lowest packing density (53.9%), while powder 6 achieves the highest packing density (60.3%) [23]. A low packing density could potentially contribute to the formation of pores in the final part due to the increased presence of voids within the powder layer [39–41]. However, during the printing phase, no visible defects were observed during the powder spreading process. Therefore, all powders exhibit sufficient flowability for regular printing.

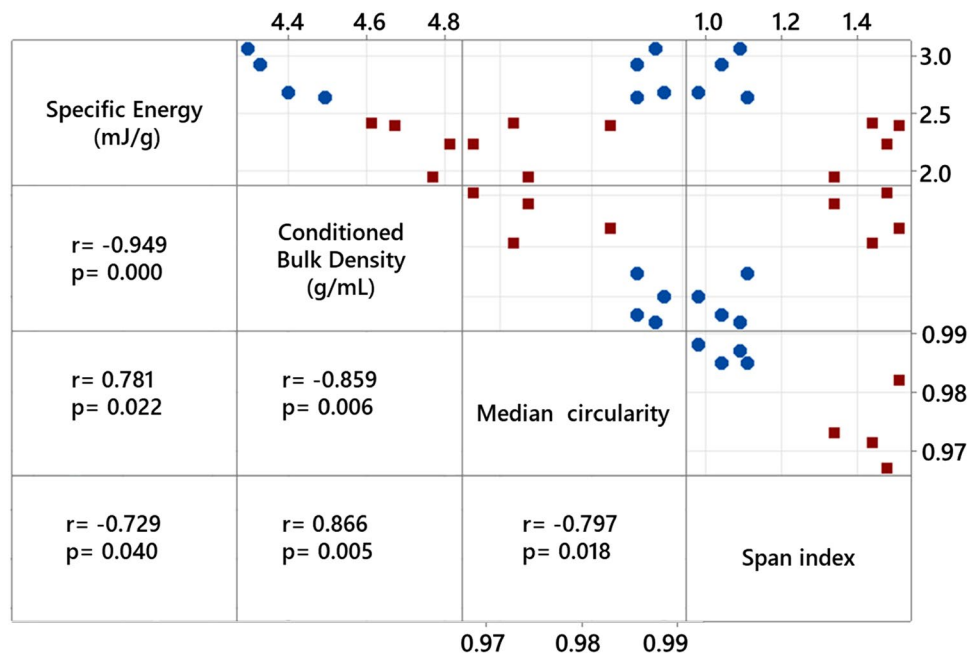
A correlation analysis is carried out to draw statistical conclusions on how PSD, shape, and flowability are connected for the eight powders under study. In addition, the Pearson coefficient between the span index (volume based), median circularity, mean SE, and mean CBD is investigated.

Figure 8 shows the strength of the linear correlation between these variables; blue circles represent powders from batch 1 powders, while red squares represent batch 2 powders. The Pearson coefficient (r) and corresponding p value are provided in the figure for each variable combination. The analysis reveals a strong correlation between all variables, indicating that particle size and shape are closely related to flowing properties.

The analysis shows that SE and CBD are linearly correlated, meaning that higher packing density implies low flowability. Powders with higher median circularity show lower flowability and lower CBD. The results contrast with the literature; however, the differences in median circularity between the powders are quite small, ranging from 0.97 to 0.99. It is plausible that, in this specific case, the variations in CBD and SE are primarily driven by the significant differences in size distribution rather than shape distribution. A similar outcome was observed by [42] for titanium powders. The span index displays a strong correlation with CBD and a weaker correlation with SE. The absolute variation in CBD is much smaller compared to SE, suggesting that the SE index is more sensitive in detecting differences among the powders. The powder characterization provided the following results:

- The shape of the PSD changes depending on the nozzle configuration and GMR. Increasing the gas flow rate

Fig. 8 Correlation between specific energy, conditioned bulk density, D_{50} circularity (volume based) and span index (volume based). The Pearson coefficient (r) and corresponding p value are provided in the figure for each variable combination



leads to a higher production of fine particles due to the increased collision probability in the atomization chamber.

- GMR also influences circularity, particularly for larger particles, due to the presence of satellites. Specifically, lower GMR results in slightly more circular powders.
- Powders from batch 2 (produced with the enhanced nozzle) show high flowability (low SE) and good packing density (high CBD). The high flowability and improved packing density are expected to enhance the mechanical properties of the printed parts.

4 Processability of powders

The tensile properties are presented in Fig. 9, where the bars represent one standard error from the mean. Five tensile specimens were tested for each powder, except for powder 4 and powder 3, which had four tests due to non-compliance

with the standards (fracture occurred outside the gauge length). For this reason, all data in Fig. 9 are calculated based on five tensile tests, except for powder 3 and 4, which are based on four tests. The overall tensile results are summarized in Table 10 in the Appendix.

The results of the tensile tests clearly indicate a difference between the powders from batch 1 and batch 2. The ultimate tensile strength (UTS), yield strength (YS), and elongation values demonstrate superior performances for the powders produced with the enhanced ring and higher atomization yield.

According to ASTM F3184-16, the expected mechanical properties of AISI 316L processed via PBF-LB/M are UTS = 530 MPa, YS = 240 MPa, and elongation = 30% (for the annealed condition, with no indication given for as-built state). As a result, all the specimens produced using the eight powders comply with the standard.

Figure 10 displays the fracture surfaces of two reference samples, one from batch 1 and one from batch 2. Only two specimens are shown, since no discernible differences were

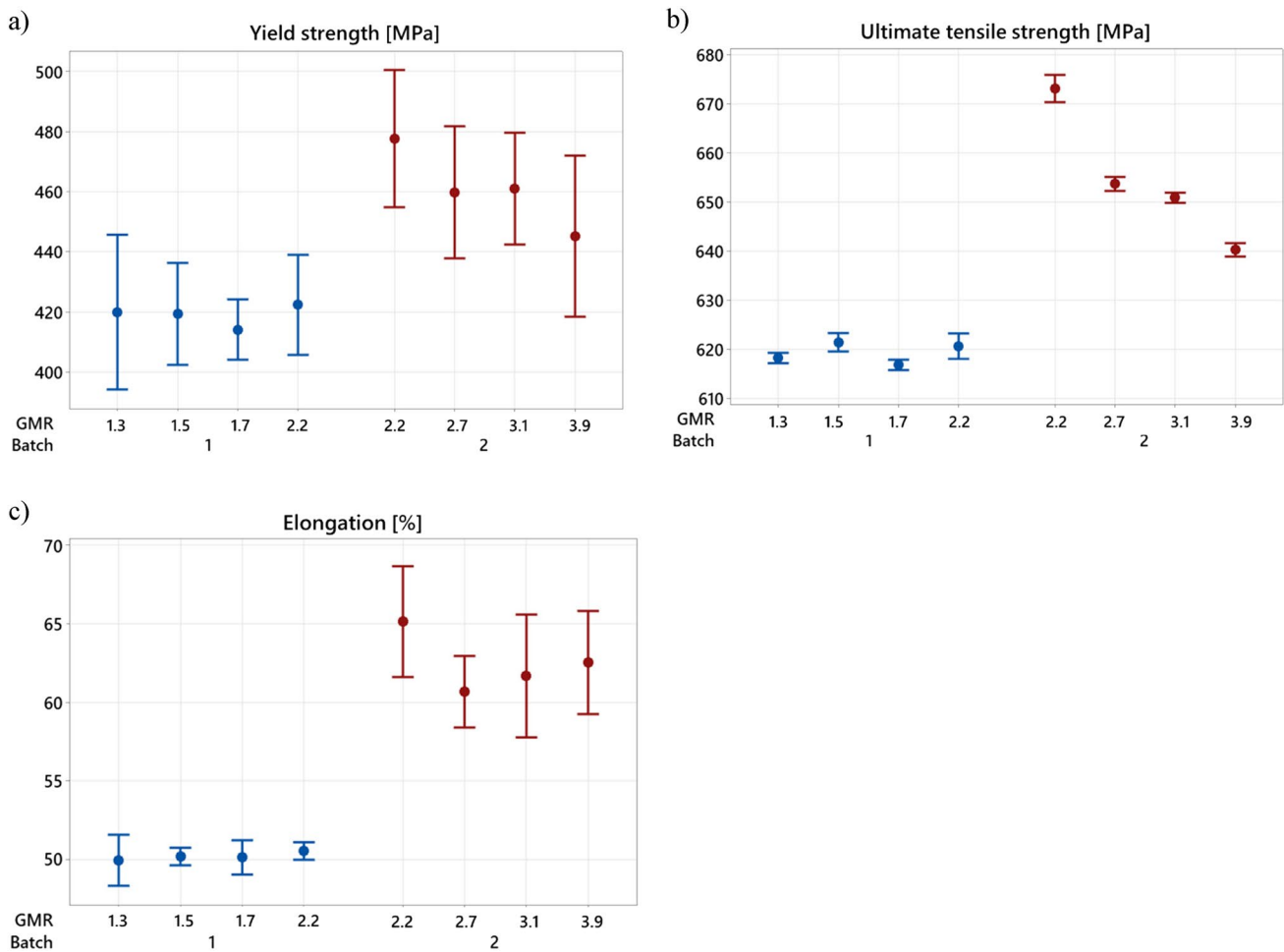


Fig. 9 Tensile properties of scrap AISI 316L produced at different GMR values. a Yield strength, b ultimate tensile strength, and c elongation

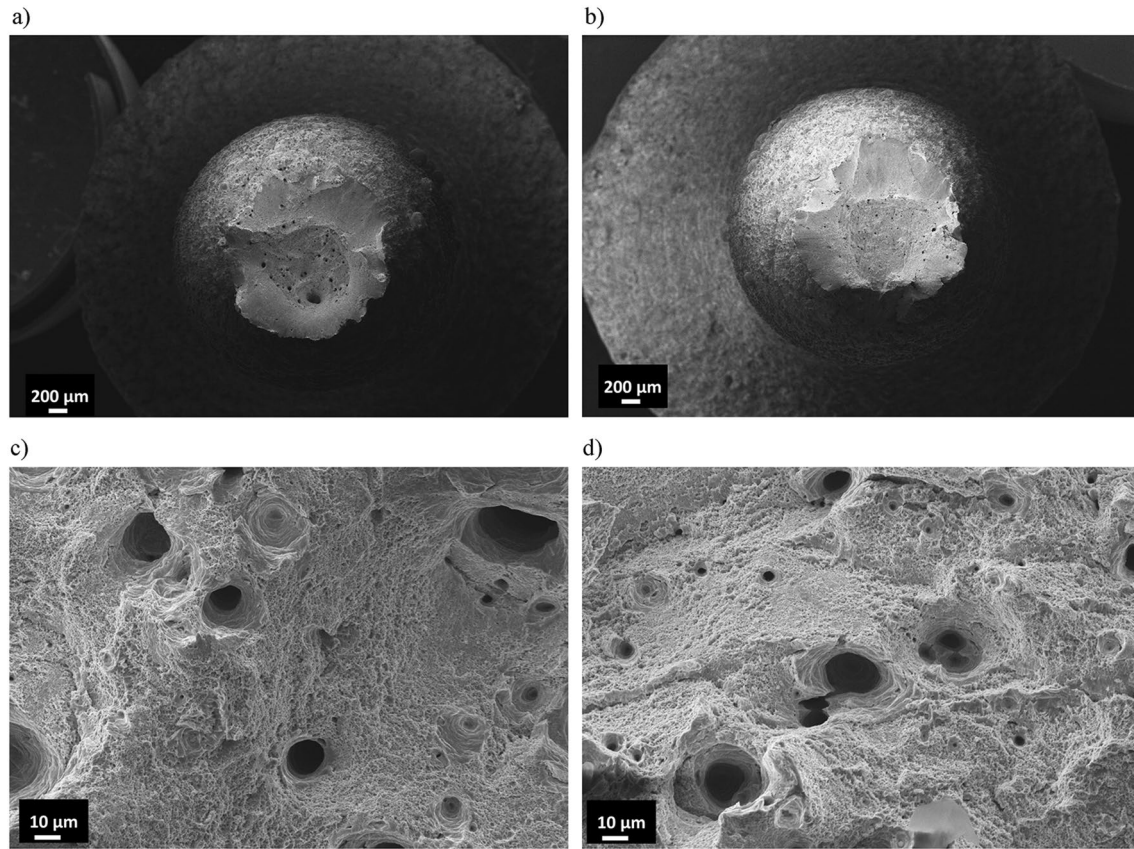


Fig. 10 Fracture surfaces from two reference samples from batch 1 and batch 2. **a** and **c** Fracture surface for a reference sample from batch 1; **b** and **d** fracture surface for a reference sample from batch 2

found among specimens within the same batch. The specimens exhibit typical ductile behavior, with extensive shear lips visible on the fracture surfaces (Fig. 10a and b).

The fractographic images of the tensile specimens (Fig. 10c and d) reveal a ductile fracture with large dimples on the surface, along with visible porosity. Figure 11 illustrates the typical defects found in the cylindrical specimens. Micro-cracks were observed, usually attributed to residual stresses induced by rapid cooling [43]. Binding defects caused by localized unmelted particles were observed; these defects are particularly detrimental to fatigue life due to their irregular shape and significant volume [44]. The size of spherical pores falls within the range of 10–20 μm , indicating the presence of gas porosity [45]. Similar defects were observed for standard AISI 316L material [46].

The microstructure of two reference samples, one from batch 1 and one from batch 2, is depicted in the optical images of Fig. 12. These images, captured parallel to the building direction, reveal similar characteristics for both powder batches. The laser scans are clearly visible, exhibiting well-defined melt pool boundaries.

ANOVA analyses were conducted to investigate the impact of GMR variation on the tensile properties. A

two-stage nested model [47] was employed for the analysis, considering the dependence of GMR values on the nozzle. The factors investigated were yield strength, UTS, and elongation, and the results of the analysis are reported in Tables 6, 7, and 8, respectively. Bold p values indicate significant factors. The Young's modulus was not included in the investigation as there was no statistically significant difference observed among the eight powders.

The ANOVA analyses reveal that batch has an influence on yield strength, elongation, and UTS. Instead, the GMR affects UTS, while its influence on elongation is relatively smaller (with a p value slightly higher than 0.05). The GMR does not influence the yield strength.

In conclusion, powders produced with enhanced atomization parameters resulted in higher mechanical properties. Also, powders produced with enhanced GMR provided mechanical properties that align with the standard AISI 316L.

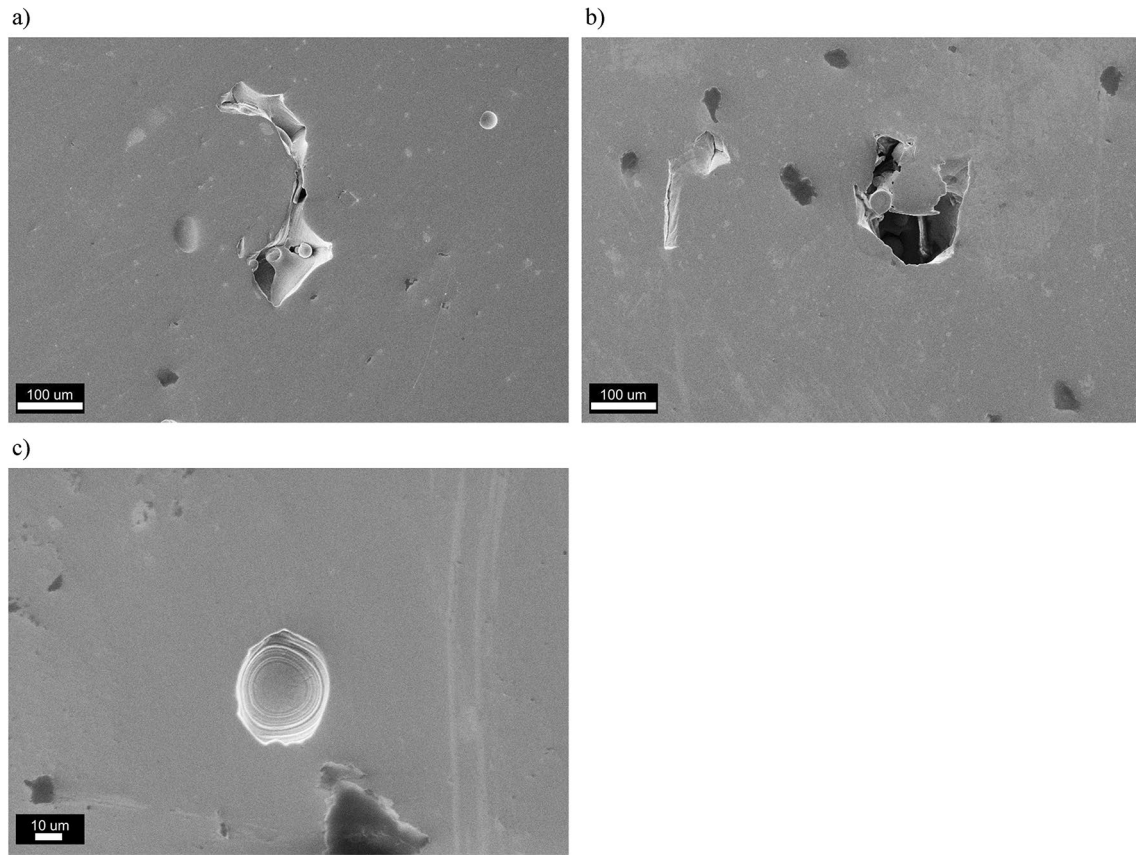


Fig. 11 Typical defects, **a** binding defects containing unmelted particles, **b** micro-crack, **c** gas pores

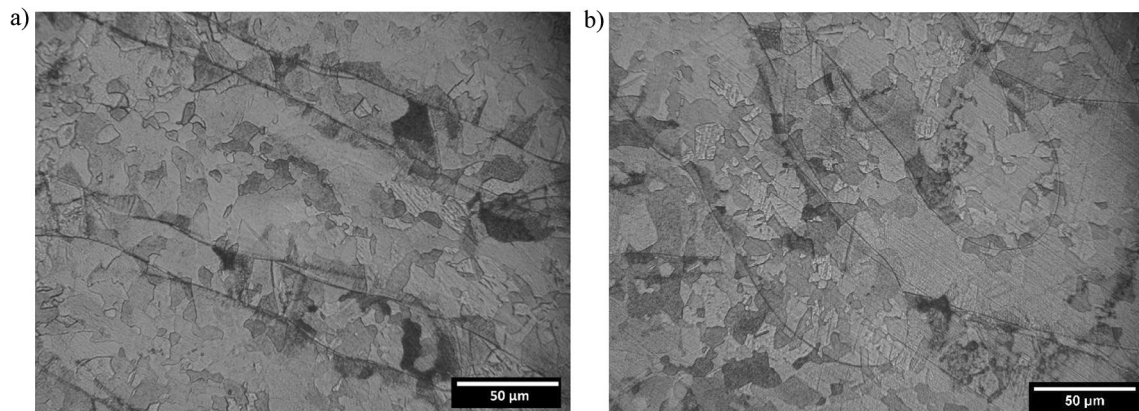


Fig. 12 Optical images of the microstructure of one reference sample from batch 1 (**a**) and one reference sample from batch 2 (**b**)

Table 6 Nested ANOVA model for the influence of batch and GMR on the yield strength, $adj-R^2=65.41\%$

Source	DF	Adj SS	Adj MS	F value	p value
Batch	1	17024	17024.1	67.26	0.000
GMR (Batch)	6	2811	468.5	1.85	0.121

Table 7 Nested ANOVA model for the influence of batch and GMR on the UTS, $adj-R^2=99.48\%$

Source	DF	Adj SS	Adj MS	F value	p value
Batch	1	12355.2	12355.2	6101.35	0.000
GMR (Batch)	6	2873.8.2	479.0	236.52	0.000

Table 8 Nested ANOVA model for the influence of batch and GMR on elongation, $\text{adj-}R^2=90.55\%$

Source	DF	Adj SS	Adj MS	F value	p value
Batch	1	1428.54	11,428.54	344.79	0.000
GMR (Batch)	6	55.56	9.26	2.23	0.070

4.1 Relationship between powder properties and tensile performance

As discussed in the previous paragraph, all powder characteristics exhibit strong correlations. Therefore, only one indicator can be used to analyze the relationship between tensile performance and powder properties. In this case, the

span index is selected due to its ease of measurement using standard methods.

The span index demonstrates a high correlation with the resulting tensile properties. Figure 13 shows that powders from batch 2 are characterized by a larger PSD and higher mechanical properties (UTS and elongation). These powders are the ones that also provide the highest yield in the atomization stage. There is a larger variation of UTS for batch 2 compared to batch 1; the variation of the PSD, circularity, or flowability could not explain this difference. Nevertheless, the difference in UTS within batch 2 is 5%, while in batch 1 is 0.8%. From an engineering perspective, these variations do not have a significant impact. The variability of the elongation results is comparable for batch 1 and 2.

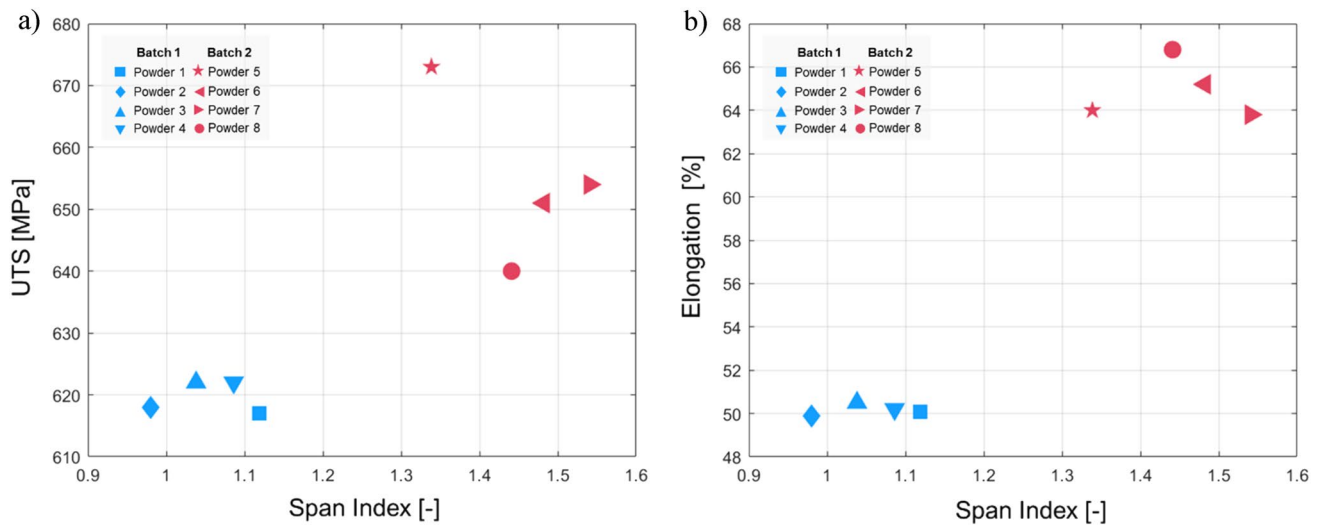


Fig. 13 Relationship between span index and tensile properties: **a** UTS and **b** elongation. For each powder, the average span index, the average of the UTS, and elongation results were plotted

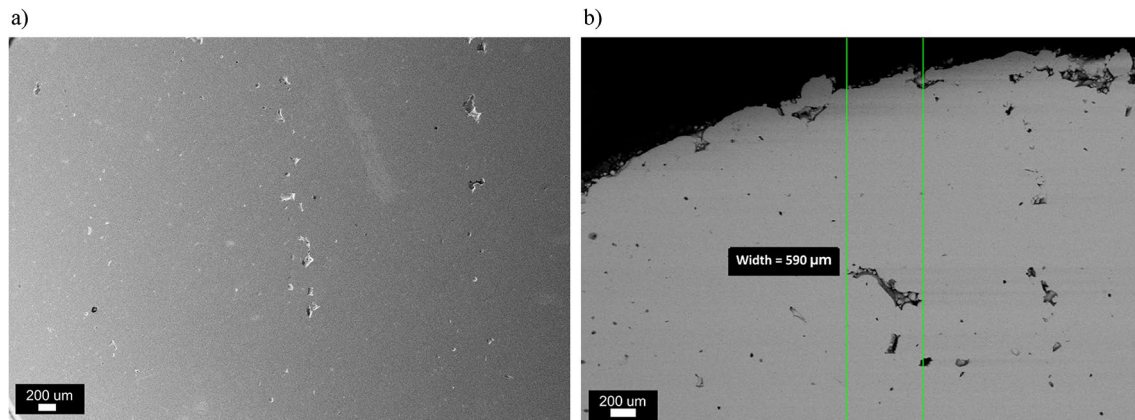


Fig. 14 Defects found on specimens produced with powder 4. **a** Pores aligned on the scan direction, **b** large lack-of-fusion pores

As mentioned in the result section, one specimen of powder 4 and one of powder 3 resulted in non-compliant tensile tests. Therefore, a further analysis was conducted on the cylindrical specimens produced using these powders. The SEM images of the polished sections are presented in Fig. 14 (images only from powder 4 are provided as a reference). The low flowability and low CBD of powder 4 could account for the presence of aligned pores (Fig. 14a) and large lack-of-fusion pores (Fig. 14b) [48]. The low SE resulted in non-uniform powder bed uniformity, which may have caused these types of defects in the final part.

5 Conclusion

This study aims to investigate how to increase the yield of the atomization process to produce powder within the PBF-LB/M range (15–60 μm). To achieve this, a prototype VIGA plant was used to produce eight powders from scrap AISI 316L material. Four powders (batch 1) were produced with the standard nozzle configuration allowing a maximum GMR of 2.2. An improved nozzle configuration was employed in batch 2, resulting in increased gas flow and a GMR of 3.9. Five tensile specimens were built for each powder to examine their mechanical performances.

The main findings of this research can be summarized as follows:

- The yield of the atomization process was improved by almost 50% (from 38 to 57%). The increased GMR resulted in powders with a narrower particle size distribution (batch 2) and with a large number of smaller particles. Batch 1 exhibited higher particle circularity, especially for larger particles.
- The flowability characterization provided results in partial contrast with the literature. Batch 2 powders, despite

the higher number of fines and slightly lower circularity, resulted in higher specific energy (meaning better flowability). At the same time, the packing density (CBD measurement) of batch 2 is improved due to the favorable arrangement of fine and large particles.

- Statistical analysis was carried out to investigate the nozzle configuration effect and the GMR effect on the mechanical properties. This study revealed that the nozzle configuration had the most significant impact on UTS, yield strength, and elongation, while the GMR only influenced UTS. Nevertheless, all the powders investigated in this work exhibited mechanical properties higher than the expected values for standard AISI 316L processed using PBF-LB/M process.
- There was a strong correlation observed between the tensile properties and powder characteristics, indicating that powders with higher flowability and bulk density exhibited higher mechanical properties. This finding suggests the potential for predicting mechanical properties based on powder characteristics, although further studies are required to draw definitive conclusions.

A direct connection was found between powder packing density and defects. The low packing density of powders 3 and 4 allowed us to understand the presence of large lack-of-fusion pores in the final parts, which resulted in non-compliant tensile tests. This result underscores the importance of powder packing density in producing defect-free PBF-LB/M parts.

Future research should study the correlation between powder flowability, powder size, shape distributions, and defect formation. Further investigation, preferably using other materials, are recommended to generalize these results

Table 9 Summarized statistics of the volume-based (V) and number-based (N) particle size distribution and circularity of the 8 powders

Batch	Powder	D ₁₀ (μm)		D ₅₀ (μm)		D ₉₀ (μm)		Circularity D ₁₀		Circularity D ₅₀		Circularity D ₉₀	
		V	N	V	N	V	N	V	N	V	N	V	N
1	1	20.3	2.7	37.8	16.8	62.6	34.0	0.897	0.928	0.969	0.985	0.993	0.995
	2	18.3	7.6	34.0	16.5	51.7	33.2	0.902	0.935	0.977	0.988	0.994	0.996
	3	19.6	7.4	34.1	19.4	55.0	34.6	0.894	0.921	0.968	0.985	0.993	0.995
	4	18.5	8.7	33.4	17.7	54.8	33.1	0.899	0.930	0.973	0.987	0.994	0.996
2	5	12.5	1.7	28.8	4.7	51.0	16.9	0.891	0.917	0.962	0.973	0.992	0.994
	6	13.7	2.0	34.0	5.6	64.0	18.1	0.891	0.904	0.960	0.967	0.992	0.993
	7	12.6	1.9	32.6	4.8	62.8	15.6	0.885	0.933	0.957	0.982	0.992	0.995
	8	14.2	1.8	32.2	5.6	60.5	19.3	0.898	0.904	0.965	0.972	0.992	0.994

Two replicates of the Morphologi measurements were performed for each powder, and the mean value is reported here

Table 10 Tensile properties of all specimens tested for the study

Powder	E [MPa]	YS [MPa]	UTS [MPa]	e [%]
1	167980	400	617	49.3
	215577	418	616	50
	153793	420	616	49.3
	167628	416	617	51.3
	162115	417	618	50.7
2	137850	431	619	50
	155309	400	618	51.7
	156524	435	619	50
	175810	414	617	50
	144889	420	618	48
3	179405	411	621	50.7
	169994	425	622	50
	141458	412	622	50.7
	126267	444	617	*
	183265	420	621	50.7
4	212292	433	622	50
	224860	408	623	50
	160384	405	619	*
	157197	434	621	50
	152637	417	622	50.7
5	176006	459	670	68.3
	177316	471	672	60.7
	144162	469	674	66.7
	179188	482	676	65.3
	163162	507	673	64.7
6	188291	449	651	58
	157220	450	650	66.7
	181378	486	651	60.7
	175630	459	652	61.5
	175624	461	650	61.5
7	157240	472	654	58
	183626	439	654	60.7
	239180	473	653	60
	174035	442	652	62
	124041	473	655	62.7
8	202304	449	641	64
	194811	451	639	66
	161085	475	641	59.3
	215261	434	641	60.7
	125794	417	639	62.7

and gain a deeper understanding of how powder properties influence the process. Additionally, the feasibility of further increasing the GMR values to improve process yield should be explored.

Appendix

Acknowledgements This work was supported by European Union, Repubblica Italiana, Regione Lombardia and FESR for the project MADE4LO under the call “POR FESR 2014-2020 ASSE I—AZIONE I.1.B.1.3”. The Italian Ministry of Education, University and Research is acknowledged for the support provided through the Project “Department of Excellence LIS4.0—Lightweight and Smart Structures for Industry 4.0”. The authors thank RINA CSM for the powder production, and Attilio Righini and Davide Lainati for the powder characterization.

Funding Open access funding provided by Politecnico di Milano within the CRUI-CARE Agreement.

Data availability The authors declare that the data supporting the findings of this study are available within the paper. Raw data are available from the corresponding author on reasonable request.

Declarations

Conflict of interest On behalf of all authors, the corresponding author states that there is no conflict of interest.

Open Access This article is licensed under a Creative Commons Attribution 4.0 International License, which permits use, sharing, adaptation, distribution and reproduction in any medium or format, as long as you give appropriate credit to the original author(s) and the source, provide a link to the Creative Commons licence, and indicate if changes were made. The images or other third party material in this article are included in the article's Creative Commons licence, unless indicated otherwise in a credit line to the material. If material is not included in the article's Creative Commons licence and your intended use is not permitted by statutory regulation or exceeds the permitted use, you will need to obtain permission directly from the copyright holder. To view a copy of this licence, visit <http://creativecommons.org/licenses/by/4.0/>.

References

- Haghdadi N, Laleh M, Moyle M, Primig S (2021) Additive manufacturing of steels: a review of achievements and challenges. *J Mater Sci* 56:64–107. <https://doi.org/10.1007/s10853-020-05109-0>
- Baumers M, Holweg M (2019) On the economics of additive manufacturing: experimental findings. *J Oper Manag* 65:794–809. <https://doi.org/10.1002/joom.1053>
- Baumers M, Beltrametti L, Gasparre A, Hague R (2017) Informing additive manufacturing technology adoption: total cost and the impact of capacity utilisation. *Int J Prod Res* 55:6957–6970. <https://doi.org/10.1080/00207543.2017.1334978>
- Lindermann C, Jahnke U, Moi M, Koch R. Analyzing Product Lifecycle Costs for a Better Understanding of Cost Drivers in Additive Manufacturing. University of Texas at Austin; 2012. <https://doi.org/10.26153/tsw/15341>.
- Anderson IE, White EMH, Dehoff R (2018) Feedstock powder processing research needs for additive manufacturing development. *Curr Opin Solid State Mater Sci* 22:8–15. <https://doi.org/10.1016/j.cossms.2018.01.002>

6. Chen H, Cheng T, Li Z, Wei Q, Yan W (2022) Is high-speed powder spreading really unfavourable for the part quality of laser powder bed fusion additive manufacturing? *Acta Mater* 231:117901. <https://doi.org/10.1016/j.actamat.2022.117901>
7. Yousef M, Thornton AR, Luding S, Weinhart T (2021) The influence of material and process parameters on powder spreading in additive manufacturing. *Powder Technol* 383:564–583. <https://doi.org/10.1016/j.powtec.2021.01.058>
8. Fredriksson C (2019) Sustainability of metal powder additive manufacturing. *Proc Manuf* 33:139–144. <https://doi.org/10.1016/j.promfg.2019.04.018>
9. Qing Y, Guo K, Liu C, Qin Y, Zhan Y, Shuo S et al (2022) Impact of atomization pressure on the particle size of nickel-based superalloy powders by numerical simulation. *Materials* 15:1–10. <https://doi.org/10.3390/ma15093020>
10. Urionabarrenetxea E, Avello A, Rivas A, Martín JM (2021) Experimental study of the influence of operational and geometric variables on the powders produced by close-coupled gas atomisation. *Mater Design*. <https://doi.org/10.1016/j.matdes.2020.109441>
11. Urionabarrenetxea E, Martín JM, Avello A, Rivas A (2022) Simulation and validation of the gas flow in close-coupled gas atomisation process: Influence of the inlet gas pressure and the throat width of the supersonic gas nozzle. *Powder Technol* 407:117688. <https://doi.org/10.1016/j.powtec.2022.117688>
12. Li X, Zhu Q, Shu S, Fan J, Zhang S (2019) Fine spherical powder production during gas atomization of pressurized melts through melt nozzles with a small inner diameter. *Powder Technol* 356:759–768. <https://doi.org/10.1016/j.powtec.2019.09.023>
13. Schwenck D, Ellendt N, Fischer-Bühner J, Hofmann P, Uhlenwinkel V (2017) A novel convergent–divergent annular nozzle design for close-coupled atomisation. *Powder Metall* 60:198–207. <https://doi.org/10.1080/00325899.2017.1291098>
14. Cacace S, Furlan V, Sorci R, Semeraro Q, Boccadoro M (2020) Using recycled material to produce gas-atomized metal powders for additive manufacturing processes. *J Clean Prod* 268:122218. <https://doi.org/10.1016/j.jclepro.2020.122218>
15. Dawes J, Bowerman R, Trepleton R (2015) Introduction to the additive manufacturing powder metallurgy supply chain. *Johnson Matthey Technol Rev* 59:243–256. <https://doi.org/10.1595/205651315X688686>
16. Qian M (2015) Metal powder for additive manufacturing. *J Mater* 67:536–537. <https://doi.org/10.1007/s11837-015-1321-z>
17. Yadollahi A, Simsiriwong J, Thompson SM, Shamsaei N (2016) Data demonstrating the effects of build orientation and heat treatment on fatigue behavior of selective laser melted 17–4 PH stainless steel. *Data Brief* 7:89–92. <https://doi.org/10.1016/j.dib.2016.02.013>
18. Engeli R, Etter T, Hvel S, Wegener K (2016) Processability of different IN738LC powder batches by selective laser melting. *J Mater Process Technol* 229:484–491. <https://doi.org/10.1016/j.jmatprotec.2015.09.046>
19. Sutton AT, Kriewall CS, Leu MC, Newkirk JW (2016) Powders for Additive Manufacturing Processes: Characterization Techniques and Effects on Part Properties. *Solid Freeform Fabrication Proceedings*. p. 1004–30
20. Slotwinski JA, Garboczi EJ, Stutzman PE, Ferraris CF, Watson SS, Peltz MA (2014) Characterization of metal powders used for additive manufacturing. *J Res Nat Inst Stand Technol* 119:460–493. <https://doi.org/10.6028/jres.119.018>
21. Clayton J, Millington-Smith D, Armstrong B (2015) The application of powder rheology in additive manufacturing. *JOM* 67:544–548. <https://doi.org/10.1007/s11837-015-1293-z>
22. Fu X, Huck D, Makein L, Armstrong B, Willen U, Freeman T (2012) Effect of particle shape and size on flow properties of lactose powders. *Particuology* 10:203–208. <https://doi.org/10.1016/j.partic.2011.11.003>
23. Fereiduni, Ghasemi, Elbestawi (2019) Characterization of composite powder feedstock from powder bed fusion additive manufacturing perspective. *Materials* 12:3673. <https://doi.org/10.3390/ma12223673>
24. Balbaa MA, Ghasemi A, Fereiduni E, Elbestawi MA, Jadhav SD, Kruth J-P (2021) Role of powder particle size on laser powder bed fusion processability of AlSi10Mg alloy. *Addit Manuf* 37:101630. <https://doi.org/10.1016/j.addma.2020.101630>
25. Kumar GS, Satishwar M, Sharma AR, Palit M, Sarkar R, Ghosal P et al (2022) Particle size dependent microstructure evolution of inert gas atomized nickel base superalloy powders. *J Alloy Compd* 909:164772
26. Luo S, Wang H, Gao Z, Wu Y, Wang H (2021) Interaction between high-velocity gas and liquid in gas atomization revealed by a new coupled simulation model. *Mater Des* 212:110264
27. Iams AD, Gao MZ, Shetty A, Palmer TA (2022) Influence of particle size on powder rheology and effects on mass flow during directed energy deposition additive manufacturing. *Powder Technol* 396:316–326. <https://doi.org/10.1016/j.powtec.2021.10.059>
28. Ma Y, Evans TM, Philips N, Cunningham N (2020) Numerical simulation of the effect of fine fraction on the flowability of powders in additive manufacturing. *Powder Technol* 360:608–621. <https://doi.org/10.1016/j.powtec.2019.10.041>
29. Shi Y, Lu W, Sun W, Zhang S, Yang B, Wang J (2022) Impact of gas pressure on particle feature in Fe-based amorphous alloy powders via gas atomization: Simulation and experiment. *J Mater Sci Technol* 105:203–213
30. Schade C, Dunkley JJ (2015) Atomization. In: Samal P, Newkirk J (eds) *Powder metallurgy*. ASM International, Ohio, pp 58–71. <https://doi.org/10.31399/asm.hb.v07.a0006084>
31. Wei M, Chen S, Liang J, Liu C (2017) Effect of atomization pressure on the breakup of TA15 titanium alloy powder prepared by EIGA method for laser 3D printing. *Vacuum* 143:185–194. <https://doi.org/10.1016/j.vacuum.2017.06.014>
32. Tan JH, Wong WLE, Dalgarno KW (2017) An overview of powder granulometry on feedstock and part performance in the selective laser melting process. *Addit Manuf* 18:228–255. <https://doi.org/10.1016/j.addma.2017.10.011>
33. Chu F, Zhang K, Shen H, Liu M, Huang W, Zhang X et al (2021) Influence of satellite and agglomeration of powder on the processability of AlSi10Mg powder in laser powder bed fusion. *J Market Res* 11:2059–2073. <https://doi.org/10.1016/j.jmrt.2021.02.015>
34. Brika SE, Letenneur M, Dion CA, Brailovski V (2020) Influence of particle morphology and size distribution on the powder flowability and laser powder bed fusion manufacturability of Ti-6Al-4V alloy. *Addit Manuf* 31:100929. <https://doi.org/10.1016/j.addma.2019.100929>
35. Vock S, Klöden B, Kirchner A, Weißgärber T, Kieback B (2019) Powders for powder bed fusion: a review. *Prog Addit Manuf* 4:383–397. <https://doi.org/10.1007/s40964-019-00078-6>
36. Schulze D (2014) *Powders and bulk solids: behavior, characterization, storage and flow*. Springer, Berlin, Heidelberg. <https://doi.org/10.1007/978-3-030-76720-4>
37. Abdelwahed M, Bengtsson S, Boniardi M, Casaroli A, Casati R, Vedani M (2022) An investigation on the plane-strain fracture toughness of a water atomized 4130 low-alloy steel processed by laser powder bed fusion. *Mater Sci Eng A* 855:143941. <https://doi.org/10.1016/j.msea.2022.143941>
38. Cacace S, Semeraro Q (2020) Influence of the atomization medium on the properties of stainless steel SLM parts. *Addit*

- Manuf 36:101509. <https://doi.org/10.1016/j.addma.2020.101509>
39. Liu B, Wildman R, Tuck C, Ashcroft I, Hague R. Investigation the effect of particle size distribution on processing parameters optimisation in selective laser melting process n.d.
40. Baitimerov R, Lykov P, Zherebtsov D, Radionova L, Shultc A, Prashanth K (2018) Influence of powder characteristics on processability of AISi12 alloy fabricated by selective laser melting. *Materials* 11:742. <https://doi.org/10.3390/ma11050742>
41. Chen H, Wei Q, Wen S, Li Z, Shi Y (2017) Flow behavior of powder particles in layering process of selective laser melting: numerical modeling and experimental verification based on discrete element method. *Int J Mach Tools Manuf* 123:146–159. <https://doi.org/10.1016/j.ijmachtools.2017.08.004>
42. Pohlman NA, Roberts JA, Gonser MJ (2012) Characterization of titanium powder: microscopic views and macroscopic flow. *Powder Technol* 228:141–148. <https://doi.org/10.1016/j.powtec.2012.05.009>
43. Narasimharaju SR, Zeng W, See TL, Zhu Z, Scott P, Jiang X et al (2022) A comprehensive review on laser powder bed fusion of steels: Processing, microstructure, defects and control methods, mechanical properties, current challenges and future trends. *J Manuf Process* 75:375–414. <https://doi.org/10.1016/j.jmapro.2021.12.033>
44. Snow Z, Nassar AR, Reutzel EW (2020) Invited review article: review of the formation and impact of flaws in powder bed fusion additive manufacturing. *Addit Manuf* 36:101457. <https://doi.org/10.1016/j.addma.2020.101457>
45. Gordon JV, Narra SP, Cunningham RW, Liu H, Chen H, Suter RM et al (2020) Defect structure process maps for laser powder bed fusion additive manufacturing. *Addit Manuf* 36:101552. <https://doi.org/10.1016/j.addma.2020.101552>
46. Liverani E, Toschi S, Ceschini L, Fortunato A (2017) Effect of selective laser melting (SLM) process parameters on microstructure and mechanical properties of 316L austenitic stainless steel. *J Mater Process Technol* 249:255–263. <https://doi.org/10.1016/j.jmatprotec.2017.05.042>
47. Montgomery DC (2013) *Design and analysis of experiments*, 8th edn. John Wiley & Sons, Inc, Hoboken, NJ
48. Ziri S, Hor A, Mabru C (2022) Combined effect of powder properties and process parameters on the density of 316L stainless steel obtained by laser powder bed fusion. *Int J Adv Manuf Technol* 120:6187–6204. <https://doi.org/10.1007/s00170-022-09160-w>

Publisher's Note Springer Nature remains neutral with regard to jurisdictional claims in published maps and institutional affiliations.